Journal of Theoretical Biology 573 (2023) 111592

Contents lists available at ScienceDirect

Journal of Theoretical Biology

journal homepage: www.elsevier.com/locate/yjtbi

Choice of spatial discretisation influences the progression of viral infection within multicellular tissues

Thomas Williams [a], James M. McCaw [a,b], James M. Osborne [a,*]

[a] School of Mathematics and Statistics, University of Melbourne, Australia
[b] Centre for Epidemiology and Biostatistics, Melbourne School of Population and Global Health, University of Melbourne, Australia

ARTICLE INFO

Keywords:
Viral dynamics
Diffusion
Spatiotemporal modelling
Numerical methods

ABSTRACT

There has been an increasing recognition of the utility of models of the spatial dynamics of viral spread within tissues. Multicellular models, where cells are represented as discrete regions of space coupled to a virus density surface, are a popular approach to capture these dynamics. Conventionally, such models are simulated by discretising the viral surface and depending on the rate of viral diffusion and other considerations, a finer or coarser discretisation may be used. The impact that this choice may have on the behaviour of the system has not been studied. Here we demonstrate that under realistic parameter regimes – where viral diffusion is small enough to support the formation of familiar ring-shaped infection plaques – the choice of spatial discretisation of the viral surface can qualitatively change key model outcomes including the time scale of infection. Importantly, we show that the choice between implementing viral spread as a cell-scale process, or as a high-resolution converged PDE can generate distinct model outcomes, which raises important conceptual questions about the strength of assumptions underpinning the spatial structure of the model. We investigate the mechanisms driving these discretisation artefacts, the impacts they may have on model predictions, and provide guidance on the design and implementation of spatial and especially multicellular models of viral dynamics. We obtain our results using the simplest TIV construct for the viral dynamics, and therefore anticipate that the important effects we describe will also influence model predictions in more complex models of virus-cell-immune system interactions. This analysis will aid in the construction of models for robust and biologically realistic modelling and inference.

1. Introduction

Mathematical modelling provides a useful toolkit for studying the spread of viral infection within tissues, both *in vivo* and *in vitro*. Over a number of decades a substantial literature has evolved, driving significant progress in our understanding of the mechanisms that drive the virological and immunological dynamics of a number of viruses, including HIV (Perelson, 2002; Graw and Perelson, 2013), hepatitis C (Guedj et al., 2013; Neumann et al., 1998), SARS-CoV-2 (Sego et al., 2020; Getz et al., 2020; Hernandez-Vargas and Velasco-Hernandez, 2020), influenza (Beauchemin and Handel, 2011; Baccam et al., 2006), and oncolytic viruses (Rodriguez-Brenes et al., 2017; Paiva et al., 2009). The importance of this work has recently been made apparent by the ongoing COVID-19 pandemic. The outbreak has prompted a large output of modelling work that has aided in the development of antiviral therapies, and an understanding of disease pathogenesis (Goyal et al., 2020; Perelson and Ke, 2021; Jenner et al., 2021). An emerging trend in the field of viral dynamics is the development of spatially-resolved models (e.g., Graw and Perelson, 2013; Sego et al., 2020; Getz et al., 2020; Wodarz et al., 2012; Paiva et al., 2009). Unlike classical models for within host viral spread, which assume mean-field dynamics, usually described by ordinary differential equations (ODEs), spatial models describe the spatial distribution of infection and track the spreading front of viral invasion. Spatial models provide a more detailed account of infection and its interaction with the immune response and the predicted dynamics can often differ substantially from those obtained from comparable ODE models (Holder et al., 2011; Beauchemin and Handel, 2011). Furthermore, depending on availability of suitable spatially-resolved data to support inference, estimated parameters are also often significantly different to those estimated from non-spatial models (Holder et al., 2011; Graw and Perelson, 2013).

There are several ways of implementing spatial structure in a viral dynamics model, for example, using neighbour-based, cellular automata (CA) methods where cells are rendered explicitly (e.g., Funk et al., 2005; Beauchemin, 2006; Kumberger et al., 2018; Rodriguez-Brenes et al., 2017), or spatially-continuous partial differential equations (PDEs) (e.g., Bocharov et al., 2019, 2016; Quirouette et al., 2020).

* Corresponding author.
E-mail address: jmosborne@unimelb.edu.au (J.M. Osborne).

https://doi.org/10.1016/j.jtbi.2023.111592
Received 20 February 2023; Received in revised form 16 June 2023; Accepted 2 August 2023
Available online 7 August 2023

An increasingly popular choice of modelling structure combines the two approaches (Sego et al., 2021, 2020; Getz et al., 2020; Whitman et al., 2020; Levin et al., 2016). These multicellular models represent cells as a grid of discrete regions of space, whilst virus density is described by a PDE. Usually, extracellular virus is produced by cells in the region of the cell, and then spreads across the cell grid according to linear diffusion. This approach is based on the assumption of different spatial scales of cells and viruses, where the size of a virus is assumed to be negligible compared to the size of a cell (Sego et al., 2021, 2020).

The multicellular model structure is of particular importance to the virus dynamics literature since it addresses limitations of both CA and PDE models. Compared to pure CA models, multicellular models track the actual spatial distribution of virus, which naturally gives rise to both short- and long-range infection events where CA models are generally constrained to neighbour-based infection rules (Holder et al., 2011; Strain et al., 2002). In more detailed models, the explicit viral distribution also makes it simple to incorporate the effects of, for example, the humoral immune response (Sego et al., 2020; Getz et al., 2020). On the other hand, compared to pure PDE models, the discrete cell structure of multicellular models ensures a sharp, well-defined boundary of the infected region and naturally captures the stochasticity of infection events, making it possible to model random infection extinction, for example (Sego et al., 2020).

However, when simulating multicellular models numerically, the three spatial scales that are present – virus, cells, and the size of the tissue or computational domain – introduce a layer of complexity when it comes to the discretisation of space. Consequently, the choice of spacing between discrete nodes or elements for the approximate viral surface (which we denote by Δx) is non-trivial. This is because, whilst traditional numerical analysis would demand that a sufficiently refined discretisation should be used to ensure convergence of the PDE, it is unclear at what scale – relative to the spacing of the cell grid – sufficient convergence is achieved. Conversely, it is not clear *a priori* at what point, or under which conditions, model predictions start to become unreliable, or precisely how model behaviour might be affected by the choice of spatial discretisation. The cell spacing is an important reference here since most of the measurable outcomes of the simulation, as well as available experimental data, occurs at the cell scale (Whitman et al., 2020; Wodarz et al., 2012; Rodriguez-Brenes et al., 2017). Should Δx be set far smaller than a cell diameter, convergence of the virus PDE may be assured, however, in such a case, the observable outcomes of the model might be influenced by viral transport or dynamics on sub-cellular length scales, which may be beyond the intended scope of the modelling framework. By contrast, a model with cell-scale or coarser discretisation may represent viral transport in a manner more consistent with the assumptions of the model, however, the resultant error from the coarser discretisation may impact the outcomes of the model. It is for this reason that the choice of spatial discretisation is important in the design of spatial virus dynamics models, and why its discussion lies beyond the scope of traditional convergence analysis.

Existing works in the literature that aim to systematically address the design and implementation of virus dynamics models involving these multiple spatial scales have mainly focused on the role of the viral diffusion coefficient (Holder et al., 2011; Gallagher et al., 2018; Funk et al., 2005; Sego et al., 2021; Strain et al., 2002). These works have shown that the sensitivity of model dynamics to the spatial structure of infection is reduced as viral diffusion increases, and discussed how viral diffusion influences key model behaviour such as the basic reproduction number ($\mathcal{R}_0$) and long-time infection outcomes (Sego et al., 2021; Funk et al., 2005; Strain et al., 2002). However, although these works highlight the highly sensitive nature of spatial phenomena in low-diffusion schema, to our knowledge there is no work in the virus dynamics literature that considers the influence of the resolution of spatial discretisation on these model outcomes.

In this work, we investigate the role of spatial discretisation through a number of experiments and simulations using a multicellular implementation of the foundational model of viral dynamics. We demonstrate realistic parameter settings under which the choice of spatial resolution in the discretised virus density (described by Δx) has a tangible and qualitative impact on a variety of key model predictions, including the computed $\mathcal{R}_0$ and the timescale of infection. We investigate the mechanisms driving these effects and the conditions under which they arise. Our results show that the choice of numerics cannot be ignored in the implementation of even the most fundamental multicellular models of viral dynamics, and we therefore anticipate that the numerical effects that we describe here are relevant to more complex models with greater biological realism at the cutting edge of the field, such as those that describe complex tissue and immune mechanisms (Beauchemin and Handel, 2011). We provide some guidance for the development and selection of spatially explicit multicellular models capable of incorporating this greater level of biological detail, which will ensure that biological modelling and inference from these systems is robust and accurately reflects the spatial structure assumed by the model.

2. Methods

2.1. The TIV model and its agent-based form

The standard model of virus dynamics within the host is the so-called TIV model, a simple but extremely robust ODE model of viral dynamics derived from mass-action kinetics (Michael Lavigne et al., 2021). The model has been well studied and applied to a wide variety of viral infections, including HIV (Perelson, 2002 provides a review), Hepatitis C virus (e.g., Neumann et al., 1998), influenza (e.g., Beauchemin and Handel, 2011; Baccam et al., 2006), and SARS-CoV-2 (e.g., Hernandez-Vargas and Velasco-Hernandez, 2020; Du and Yuan, 2020), and yielded useful estimations of biological parameters in each case. We assume a population of target cells T and infected cells I, as well as a global measure of extracellular viral load V. Target cells are assumed to become infected by virus at a rate β, infected cells are assumed to die at a rate δ, and virus is produced by infected cells at rate p, and is cleared at rate c. These assumptions are deceptively powerful, since, for example, infected cell and virus clearance rates can implicitly account for effects of immune clearance. Some presentations of the TIV model include birth and death phenomena of target cells, however, here we will assume such effects are negligible, which is common for models of acute infections (Smith and Perelson, 2011). The model under these assumptions has the following form:

$$\frac{d}{dt}\left(\frac{T}{N}\right) = -\beta\frac{T}{N}V, \tag{1}$$

$$\frac{d}{dt}\left(\frac{I}{N}\right) = \beta\frac{T}{N}V - \delta\frac{I}{N}, \tag{2}$$

$$\frac{dV}{dt} = pI - cV. \tag{3}$$

Here $N = T_0 + I_0$, where T_0 is the initial number of target cells and I_0 is the initial number of infected cells. Typically I_0 is small (or zero) and thus $N \approx T_0$. Including dead cells, N represents the total number of cells in the model. As such, in this form, the model tracks the proportion of the cell population comprised of target cells and infected cells over time. Analysis has shown that much of the behaviour of the model depends on the basic reproduction number $\mathcal{R}_0 = \beta p T_0/(\delta c)$ (assuming $I_0/N \approx 0$) (Michael Lavigne et al., 2021; Beauchemin and Handel, 2011). $\mathcal{R}_0$ defines the number of infected cells produced by a single infected cell during its lifetime (Diekmann et al., 2010). As such, when $\mathcal{R}_0 < 1$, the infection will die out, whereas if $\mathcal{R}_0 > 1$ an infection can be established (Baccam et al., 2006).

Since we are interested in finding a spatially explicit multicellular equivalent of Eqs. (1)–(3), we now define cells as explicit, individual agents that occupy regions of physical space, and can be in one of

three states: uninfected (T), infected (I), or dead (D). We associate with each cell, living or dead, an index $i \in \{1, 2, \dots N\}$. We assume that the cells are arranged in a regular grid that tessellates the spatial domain of study, Ω, resulting in a confluent monolayer of cells similar to an *in vitro* assay. Here we assume cells are simply arranged in a rectangular grid, where each cell is assumed to be a unit square. It is worth mentioning that a more precise formulation would be to assume a hexagonal grid, which has been applied in a number of other, agent-based models of viral infections and more accurately represents the packing of epithelial cells in a confluent monolayer (Whitman et al., 2020; Holder et al., 2011; Kumberger et al., 2018; Blahut et al., 2021). However, as explained below in our discussion of numerical implementation, for simplicity we discretise the viral surface using a rectangular mesh throughout this work, and therefore, for the purposes of our investigation of numerical discretisation, it will be sufficient and markedly more intuitive to use a rectangular cell grid. Nonetheless, we have also repeated our experiments for a hexagonal cell grid (and a rectangular viral mesh) with qualitatively the same results (figures in Supplementary Information). We do not anticipate that our results will be qualitatively any different for other configurations of either the cell grid or the viral mesh.

Following standard assumptions of the literature (Gallagher et al., 2018; Sego et al., 2020, 2021), we model the virus population of the system as a density distribution of extracellular virions, which are produced uniformly over the domain of infected cells, and spread throughout the computational domain according to linear diffusion. As such, the virus equation, Eq. (3), becomes the PDE

$$\frac{\partial v}{\partial t} = p \sum_{i \in I} \frac{\mathcal{X}_{S_i}(\mathbf{x})}{|S_i|} - cv + D\nabla^2 v, \tag{4}$$

where we write I for the set of infected cells, S_i for the region of space occupied by cell i, and D for the diffusion coefficient. $\mathcal{X}_S(\mathbf{x})$ is the characteristic function

$$\mathcal{X}_{S_i}(\mathbf{x}) = \begin{cases} 1, & \mathbf{x} \in S_i, \\ 0, & \mathbf{x} \notin S_i. \end{cases}$$

It is straightforward to verify that integrating Eq. (4) over Ω, subject to appropriate boundary conditions, recovers the ODE form of the virus equation.

To replace the target cell and infected cell equations, Eqs. (1) and (2), with update rules for individual cells, we consider the Poisson process of the number of state transitions in a given time interval t. We consider the simple case of the transition from infected cell to dead cell, $I \to D$. Infected cell death occurs at rate δ, so for a given infected cell i, the probability that it does *not* die in a given time interval Δt is given by the following:

$$P(\sigma_i(t + \Delta t) = I \,|\, \sigma_i(t) = I) = e^{-\delta \Delta t},$$

where we adopt the notation $\sigma_i(t) \in \{T, I, D\}$ for the state of cell i at time t. Since infected cells can either die or stay infected in a given time step, we conclude that the transition probability is

$$P(\sigma_i(t + \Delta t) = D | \sigma_i(t) = I) = 1 - e^{-\delta \Delta t}. \tag{5}$$

Considering the transition from uninfected cell to infected cell, $T \to I$, we apply a similar argument. Here, the rate of infection is dependent on the viral load as well as the infection parameter β. We assume that cell i can be infected by the quantity of virus in the domain of the cell, $\int_{S_i} v(\mathbf{x}, t) d\mathbf{x}$, and that this quantity has negligible change over the small time interval Δt. However, by only considering the viral load within cell domain S_i, rather than the global domain Ω, we effectively shrink the tissue size by a factor of $|S_i| / |\Omega| = 1/N$. Since β is a contact parameter and depends on the size of the cell population, we must the rescaling $\beta \to \beta N$ in order to preserve the dynamics of the original system (for details, see the Supplementary Information). The effective rate of infection is therefore $N\beta \int_{S_i} v(\mathbf{x}, t) d\mathbf{x}$, and using the argument above, we obtain the transition probability for infection:

$$P(\sigma_i(t + \Delta t) = I \,|\, \sigma_i(t) = T) = 1 - \exp\left(-N\beta \int_{S_i} v(\mathbf{x}, t) d\mathbf{x} \Delta t \right). \tag{6}$$

Collectively, Eqs. (4)–(6) govern the agent-based form of the model. We apply periodic boundary conditions on opposite sides of the computational domain to eliminate boundary effects.

Table 1
Fixed parameters used in our simulations (derived from Hernandez-Vargas and Velasco-Hernandez, 2020).

Description	Symbol	Value and units
Infection rate	β	1.83×10^{-5} (copies/ml)$^{-1}$ h^{-1}
Death rate of infected cells	δ	4.33×10^{-2} h^{-1}
Virion production rate	p	2.23×10^{-1} cell^{-1} h^{-1}
Viral clearance rate	c	0.1 h^{-1}
Number of cells	N	14,400 (120 × 120 grid)

Since our aim in this work is qualitative and not a sensitivity analysis per se, our approach to parametrisation is as follows. For the parameters β, δ, p, and c, we use the following indicative parameter set throughout this work, which is taken from values found in Hernandez-Vargas and Velasco-Hernandez (2020) (with β rescaled appropriately for the number of cells in our model). In this paper, Hernandez-Vargas and Velasco-Hernandez fit the TIV model, Eqs. (1)–(3) to data from human COVID-19 patients. Clearly, adapting this model to a spatial context and introducing viral diffusion modulates the behaviour of the system compared to its ODE form, but these parameter values are nonetheless sufficiently biologically realistic for the purposes of this work.

The choice of diffusion coefficient, D has a profound influence on the qualitative outcome of model simulations as well as numerical requirements, as we shall see. However, the question of which diffusion coefficient is most appropriate in a given scenario does not have a straightforward answer (Gallagher et al., 2018). The kind of spatial data required to calibrate the viral diffusion coefficient is in limited supply, and as such D is usually inferred from other, potentially conflicting sources (Gallagher et al., 2018). *In vitro* infection assays for most viruses, for example, show the formation of tight viral plaques, with ring-shaped infection fronts, that suggest a fairly small diffusion coefficient (Wodarz et al., 2012; Chiem et al., 2021; Holder et al., 2011). There is also evidence from *in vivo* experiments which suggest highly localised spread of virus. Work by Fukuyama and colleagues, which studied mice infected with multiple differently-coloured fluorescent reporter influenza viruses, showed the formation of single-coloured clusters of infected cells, suggesting virus had spread locally from the first infected cells (Fukuyama et al., 2015). On the other hand, estimations of the diffusion coefficient using the Stokes–Einstein equation, based on viral particle diffusion in mucus, suggests a larger value for D (Holder et al., 2011; Sego et al., 2020). Moreover, a larger diffusion coefficient would explain long-range viral dispersal through sections of tissue within the host, for example the respiratory tract. These conflicting phenomena make it challenging to fix a value for D. For this reason, we approach the choice of D qualitatively rather than quantitatively.

In Fig. 1, we demonstrate the infection patterns formed from a single source cell under three biologically plausible scales for the diffusion coefficient, and also show the results of the equivalent ODE system, Eqs. (1)–(3), with the same parameters. As mentioned, due to the challenges in exactly specifying D in a given context – especially given that its effects are modulated by the choice of other parameters – it is difficult to discuss the range of values for D in absolute, quantitative terms. Therefore we use Fig. 1 as a reference point for qualitatively small and large values of D. Crucially, at small- and medium-scale diffusion ($D = \mathcal{O}(10^{-1} - 10^{0})$ CD^{2}h^{-1}) (where CD is a typical Cell

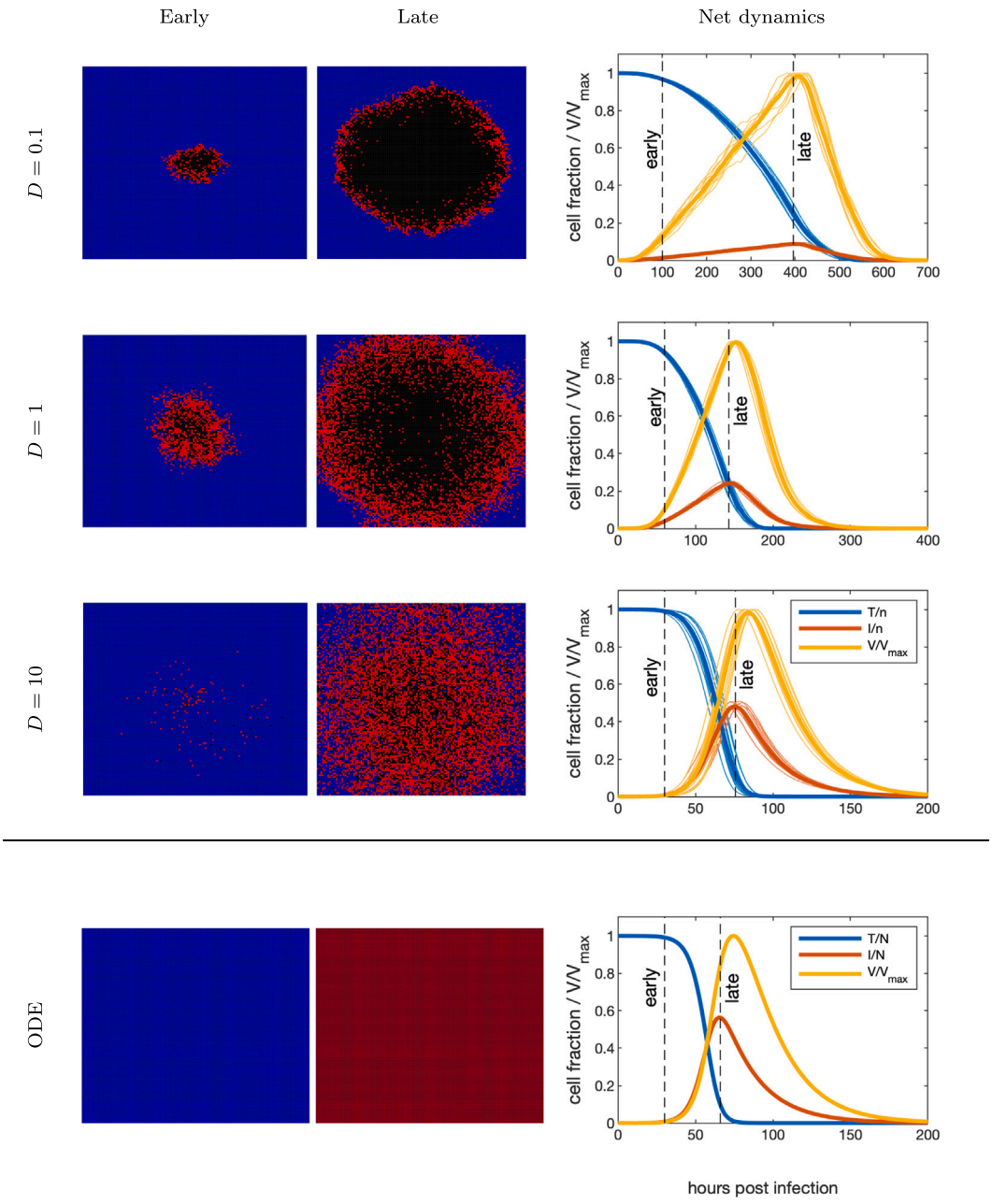

Fig. 1. The multicellular TIV model under the parameters in Table 1 and different diffusion coefficients (units of $CD^2\ h^{-1}$), compared with the dynamics of the analogous ODE form of the model. For each choice of diffusion coefficient, we initiate the multicellular model with a single infected cell in the centre of the grid. In the left two columns is the state of the cell grid early in the infection and near the peak infected cell fraction. Target cells are shown in blue, infected cells in red, and dead cells in black. For the ODE case, we shade the entire grid according to the proportions of each cell type using the same colour scheme. In the right column we show the net dynamics of the model with the corresponding diffusion coefficient, plotting time series of target and infected cell fractions and total viral load (normalised relative to its maximum). For the multicellular model, we plot time series for ten model simulations and also show the average in bold. Vertical dashed lines represent the "Early" and "Late" time points for that diffusion coefficient, at which the corresponding cell grid images were taken.

Diameter, here taken to be 10 μm as the size of a typical epithelial cell in the respiratory tract Devalia et al., 1990), the infection forms a distinct plaque with infected cells on the periphery and dead cells at the centre. As diffusion increases, this pattern is distorted to become increasingly uniformly distributed. In the case of large diffusion, for example $D = \mathcal{O}(10^1)\ CD^2h^{-1}$, the ring structure is lost, conditions become well-mixed, and the model behaviour rapidly converges to the ODE solution. We will conduct most of our analysis here using $D = 0.1\ CD^2h^{-1}$ and $D = 1\ CD^2h^{-1}$.

2.2. Numerical implementation

We simulate our model by updating the state of both the cell grid and the virus density every small time step Δt. If we set $\mathcal{G}_\tau$ to be the state of the cell grid and $\mathbf{v}_\tau$ to be the numerical virus density surface at discrete time τ, then with each time step we do the following:

At the start of a given time step at time τ, we begin by checking every cell in the simulation for a state transition and generate the next state of the cell grid $\mathcal{G}_{\tau+\Delta t}$ based on the state of the virus surface and

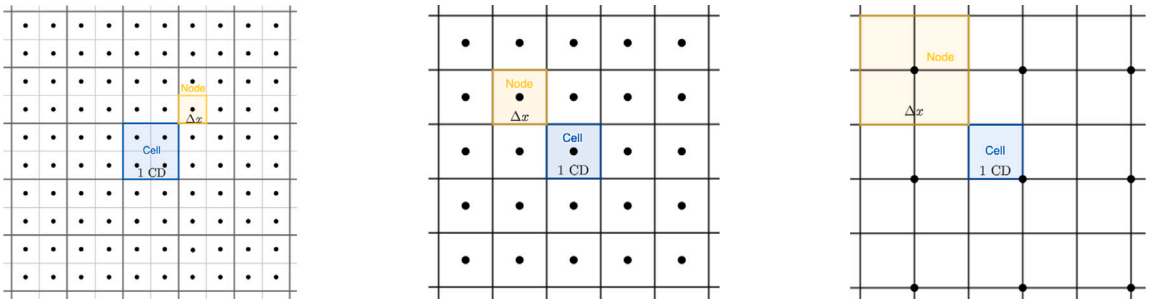

(a) Fine mesh. Here $\Delta x = 0.5$ CD. (b) "Reference" mesh ($\Delta x = 1$ CD). (c) Coarse mesh. Here $\Delta x = 2$ CD.

Fig. 2. Alignment of the cell grid and virus mesh. Note that in the fine mesh case, each viral node uniquely belongs to one cell each, and in the coarse case, each cell uniquely belongs to one viral node each. In the reference case there is a 1-1 correspondence between cells and nodes.

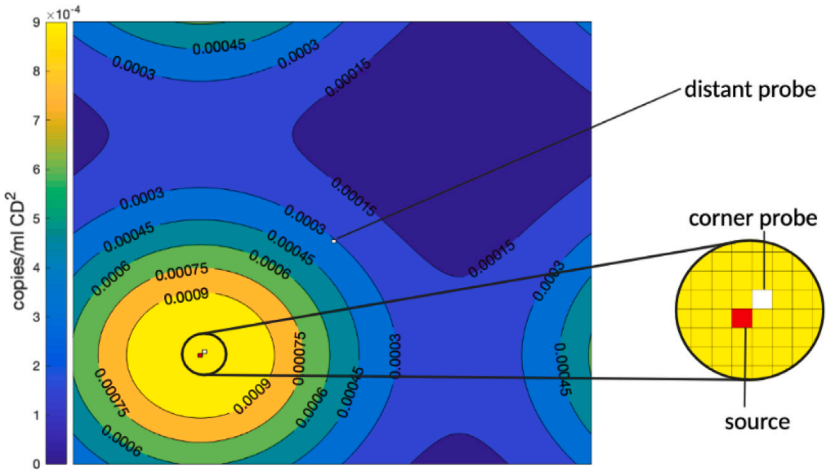

Fig. 3. Demonstration of probe experiment and the placement of the source and probe cells. We plot the contours of the viral surface after $t = 50$h, using $D = 10$ CD^{2}h^{-1}.

the cell grid at the start of the time step, $\mathcal{G}_\tau$. We then update the virus density surface using a forward Euler finite difference scheme, also based on the state of the grid at the start of the time step, $\mathcal{G}_\tau$. We then update both the cell grid and the numerical virus density and increment time by Δt. Δt is chosen to satisfy the Von Neumann stability condition for the PDE, $\Delta t \leq (\Delta x)^2/(4D)$, based on our range of choices for diffusion and spatial discretisation parameters. That is, the same Δt is used for each choice of Δx for a given value of D. Following the Lax–Richtmyer Theorem this is a sufficient and necessary condition for stability (Lax and Richtmyer, 1956).

We solve the virus PDE over a finite difference mesh, which is distinct from the cell grid, although both occupy the same spatial domain Ω. We consider cells to be squares of unit length, and hence use cell widths (or *diameters*) as our unit of spatial measurement. We vary the spacing of the nodes of the PDE mesh, Δx, to investigate any influence this might have on the results of model simulations. We restrict ourselves to Δx values of the form k, or $1/k$, where $k \in \mathbb{Z}$ to avoid any ambiguities with mesh nodes lying on cell edges. That is, we consider mesh spacings that are either a whole number of cell widths apart, or an integer fraction of a cell width apart. Fig. 2 shows the alignment of the virus PDE mesh relative to the cell grid under these assumptions. For further details of the numerical implementation of our model, see the Supplementary Information. Our code is written in MATLAB and can be found on GitHub (https://github.com/thomaswilliams23/TIV_spatial_discretisation_code.git).

As this construction suggests, $\Delta x = 1$ is a special case in which the virus surface is discretised with the same spacing as the cell grid (middle plot in Fig. 2). Under such a scheme, each cell is associated with precisely one node of the extracellular viral density. We will refer to this as the "reference case" since it is the most conceptually simple scenario and as such, we will present results of altering Δx compared to this reference.

3. Results

3.1. Choice of spatial discretisation affects virus export from infected cells

The convergence of the diffusion (heat) equation for small values of Δx is a standard result in numerical methods. However, the introduction of an alternate spatial scale – the cell – necessitates a more careful discussion of convergence. We sought to understand how the numerical solution of a diffusive process could influence the amount of the diffusing material available at a cell probe, as opposed to a single point. In the context of hybrid viral models, the amount of virus available to cells as it diffuses in the domain is of particular importance, as this will influence the probability of infection.

To investigate how the spread of virus across the tissue might be influenced by the choice of refinement in the spatial discretisation, we tracked how the virus generated by a single infected cell spreads across the cell sheet during its lifetime. To do this, we made the following simplifications to the model: (i) we set a single cell to be infected, and prevented any other cells in the sheet from becoming infected, and (ii) we set viral decay $c = 0$ h^{-1}, such that the evolution of the viral density is determined only by diffusion and its source term. Simulations were initiated with no extracellular virus in the system. Moreover, after the mean infected cell lifetime $1/\delta$ h (this follows simply from the ODE form of the model, Eqs. (1)–(3)), we set the source cell to die, such that the source of virus is "turned off", and allow more time for the remaining virus to spread in the tissue.

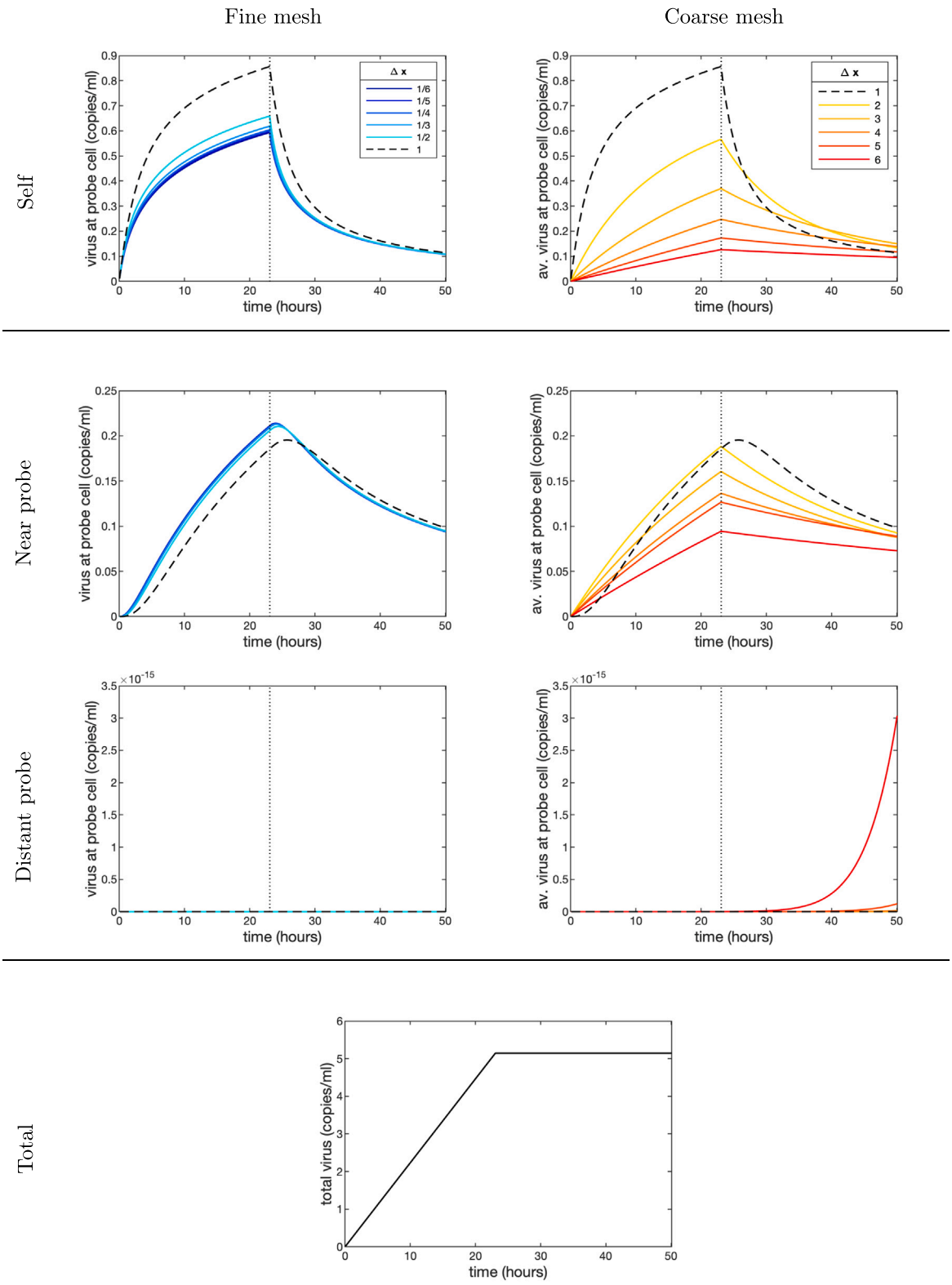

Fig. 4. Effect of choice of spatial discretisation on virus availability at two probe cells both near to and distant from a single infected source cell, as well as at the source cell itself, using $D = 0.1\ CD^2h^{-1}$. Following Hernandez-Vargas and Velasco-Hernandez (2020), viral load is given in units of copies/ml. We also plot the total viral load in the system over time, which is identical for any choice of Δx. In the case of coarse mesh refinement, we choose the probe cell at random to account for the position of the source and probe cells relative to the viral nodes, and take average behaviour across 200 simulations.

We record the viral load available to two *probe* cells over time under these conditions, as well as at the source cell itself. The two probes are chosen such that one is nearby to the source (they share a corner), and the other is relatively distant (at a diagonal distance of 30 cells). This reflects long- and short-range interactions between cells in the tissue. In Fig. 3 we show a diagram of the virus density surface after 50 h and indicate the location of the probes (note: for ease of presentation, Fig. 3 was generated using $D = 10\ \mathrm{CD^2h^{-1}}$; in the following analysis

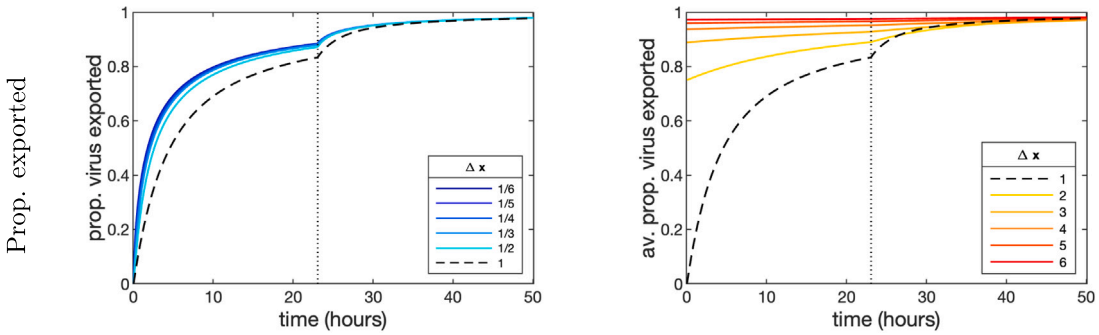

Fig. 5. Proportion of "productive" virus in system (proportion of virus external to the source cell). Here we use $D = 0.1\ CD^2h^{-1}$.

we will take $D = 0.1\ \mathrm{CD}^2\mathrm{h}^{-1}$). We repeated this experiment for a range of Δx values. In cases where the PDE mesh is coarser than the cell grid ($\Delta x > 1$), the position of the source cell relative to the configuration of the cell grid biases the amount of virus available at the probes. For example, if $\Delta x = 2$ as in Fig. 2, the diagonal neighbour (the near probe) of a given cell may correspond to the same viral node, but may also correspond to a neighbouring viral node. To account for this artefact in these cases, we chose the source cell at random and identified probe cells relative to their position, and reported the average behaviour over 200 such simulations.

Fig. 4 shows the outcome of this experiment, using a diffusion coefficient of $D = 0.1\ \mathrm{CD}^2\mathrm{h}^{-1}$. In each plot, we chart the viral load at the indicated cell over time under different choices of Δx values. In the left column of Fig. 4, we show the behaviour of the system for increasing refinement of the PDE discretisation ($\Delta x \to 0$, i.e. convergence of the model). From the plots of viral load at the near probe and the source cell, we notice that, whilst the dynamics converge as $\Delta x \to 0$, there is a significant deviation between the limit of mesh refinement and the reference case of $\Delta x = 1$, at least under our choice of a small diffusion coefficient. Our results suggest that increasing mesh refinement leads to less virus remaining at the source cell, and increases the amount of virus found at nearby cells. Note that this effect is observed even though the amount of virus produced in each case is identical, regardless of the value of Δx (see Fig. 4 Total). At the distant probe, the viral load remained negligibly low throughout the entire simulation for any value of $\Delta x \leq 1$.

In the case of coarse mesh refinement (right column of Fig. 4), model simulations rapidly diverge from the reference case ($\Delta x = 1$) as Δx increases. In particular, the viral load time series at the near probe is qualitatively different to the reference case, even for $\Delta x = 2$. At the distant probe, it can be seen that in the very coarse case, proportionally much more virus reaches the cell towards the end of the simulation. Unlike with the near probe, this divergence arises long after the source cell has died, indicating that this viral load occurs from the virus already in the system equilibrating across the sheet. This process is evidently accelerated when Δx is very large, however, is unlikely to influence the simulation in any meaningful way, since the actual *amount* of virus at this distance from the source cell is still extremely low (on the order of 10^{-15} copies/ml compared to $\mathcal{O}(10^{-1})$ copies/ml at the near probe).

As with the fine mesh case, coarse mesh refinement leaves significantly less virus at the source cell, however, here, nearby cells also tend to have access to less virus. Fig. 5 provides insight into the mechanics of this viral export process, and how it is affected by the choice of Δx. Here, we plot the proportion of the total virus in the system that is *not* found at the source cell. That is to say, we plot the proportion of virus that has been exported from the source cell. This can be considered the proportion of *productive* virus in the system at a given time: given that the source cell is already infected, any virus that remains in its vicinity cannot produce any new infections. Fig. 5 shows that the proportion of productive virus is greater than the reference case for both fine and coarse discretisation schemes. This suggests that virus is more rapidly and effectively transported from the source cell in either case, despite none of the actual model parameters being changed.

As Fig. 5 suggests, there are separate mechanisms that explain this enhanced transport in both the fine and coarse mesh cases. Where the PDE mesh resolution is coarser than the cell grid, any virus generated by an infected cell is immediately accessible to all other cells that share the same viral node. As such, only a small proportion of the virus generated by the source cell remains at the source, and the rest instantly becomes productive. This phenomenon explains the substantially and instantaneously higher proportion of exported virus for coarser mesh resolutions in Fig. 5. Moreover, as the mesh becomes increasingly sparse, more cells share in the instantaneous spread of produced virus, and the resulting viral distribution becomes broader and flatter. This explains the flattening viral load curve at the near probe and the increasing viral availability at the distant probe in Fig. 4.

The acceleration of viral transport in the fine mesh case is more subtle and does not act instantaneously. Here viral export is enhanced because, relative to the case where $\Delta x = 1$, increasing mesh refinement reduces the distance virions must travel from a cell boundary to reach adjacent cells. If cells each contain only a single viral node, virions need to travel an entire cell width to access neighbouring cells, however, if cells contain many nodes, virions need only travel a fraction the width of a cell to access the viral nodes attached to neighbours, thereby reducing the time before cells begin to experience a concentration of virus. Clearly, this "spill-over" effect is enhanced when the diffusion coefficient D is small enough that viral spread across sub-cellular length scales occurs over a non-trivial time interval. In the Supplementary Information we show that this effect is attenuated as D increases. We remark here, however, that should a modelling application demand a diffusion coefficient on the order of what we have shown in Fig. 5 (such that very fine mesh resolution ($\Delta x < 1$) is necessary to ensure convergence), the assumptions of the multi-scale model begin to break down. For example, at such a fine level of spatial detail, the packing of cells (which is closer to hexagonal than rectangular Blahut et al., 2021; Graw et al., 2015) and heterogeneity in receptor availability start to become important, and even the assumption that virus is well-approximated by a density surface begins to come under strain.

3.2. Choice of spatial discretisation influences the computed reproduction number

Having shown that changing Δx modulates the spread of virus across the tissue, we sought to demonstrate how this affects the "biology" of the model. In the Methods Section we discussed the notion of the basic reproduction number $\mathcal{R}_0$, which characterises the TIV system of ODEs. $\mathcal{R}_0$ measures the number of infections caused by a single infected cell over its lifetime, and is therefore a useful measure of viral infectivity, given the parameters of the model (Perelson, 2002; Beauchemin and Handel, 2011). Such a notion is much more challenging to define in a spatial context, since the availability of target cells is constrained by

the spatial arrangement of the tissue. This is further complicated by our use of a discrete cell grid. To circumvent much of this complexity, we here introduce an *empirical* $\mathcal{R}_0$. This quantity, for which we write $\mathcal{R}_0^*$, is simply defined as the numerically computed number of infections caused by an infected cell over its lifetime under the model.

To investigate how the choice of spatial discretisation influences $\mathcal{R}_0^*$, we ran simulations of our model using different choices of Δx. In each case, we randomly chose 1% of the cells to begin the simulation infected, and at $t = 1/\delta$ all infected cells were killed, having reached their average life span, as in the previous experiment. We allow sufficient extra time for any virus in the system at this point to cause further infections as it spreads and decays, until the probability of further infections becomes negligible. Infection events are implemented here as follows: whenever our model reports a cell becoming infected (according to the state transition probability rules), that cell is flagged to prevent becoming infected again, but does *not* go on to secrete virus. In this way, all infections in the system can be exclusively attributed to the initially infected cells. We calculate $\mathcal{R}_0^*$ as the mean number of infection events per starting infected cell. We repeated the experiment for both $D = 0.1$ CD^{2}h^{-1} and $D = 1$ CD^{2}h^{-1}.

We use multiple initially infected cells instead of a single cell for our calculations because it substantially reduces the random variation between simulations. The proportion of the cell sheet that is initially infected has been termed the multiplicity of infection or MOI (in the sense used by, e.g., Whitman et al., 2020, which differs slightly from how the term is used in the biological literature). Clearly our formulation of $\mathcal{R}_0^*$ depends on the choice of MOI (which we explore in the Supplementary Information), however, it is sufficient to show how the viral infectivity of the model is affected by change in the spatial discretisation.

In Fig. 6(b), we plot $\mathcal{R}_0^*$ values for different choices of Δx alongside error bars indicating one standard deviation. Fig. 6(b) shows that this "basic reproduction number" is increased both when Δx is smaller and when it is larger than the reference case at $\Delta x = 1$. This extends our findings from the previous result, by demonstrating that the accelerated transport of virus in both very fine and very coarse mesh schemes results in an increased number of infections. Consequently, the model predicts a higher viral invasive potential, *despite none of the actual model parameters changing*.

Again, this effect is stronger when diffusion is smaller. In the case where $D = 0.1$ CD^{2}h^{-1}, the variation in $\mathcal{R}_0^*$ is substantial and vastly exceeds the noise present in the system. When $D = 1$ CD^{2}h^{-1}, there is still an appreciable change in the basic reproduction number for varying Δx, however, this variation is proportionally less significant relative to the randomness of the system.

In Fig. 6(c), we also plot the mean of the infection time distribution for each choice of Δx. Fig. 6(c) shows that the mean infection time is reduced compared to the reference case in both fine and coarse discretisation schemes. This result follows from the finding in Fig. 4 that viral export is accelerated in these settings, and complements our $\mathcal{R}_0^*$ result by demonstrating that small and large Δx values lead to not only more infections, but also, on average, earlier infections.

However, this increase in the number of infections (reproduction number) cannot fully be explained by simply adding infections that occur earlier in the simulation. For example, comparing the $\Delta x = 1$ reference case with the $\Delta x = 2$ case, note that whilst the average infection time is significantly reduced for the coarser mesh, this barely results in any change in $\mathcal{R}_0^*$. This suggests that whilst early infections are more likely under this scheme, there must also be a *reduction* in the likelihood of infections at later times. These results point to a complex relationship between the distribution of infection times and the spatial discretisation.

We explore this relationship in the Supplementary Information. Our analysis suggests that in coarse mesh schemes, the early acceleration in infection is driven by infections of cells which share a viral node with a cell which produces virus. This eliminates viral transport time and permits rapid infections early in the simulation. However, compared to large Δx cases, where there are many target cells which share viral nodes with initially infected cells, when Δx is only slightly larger than 1, this pool is much smaller. Once availability of these cells becomes constrained, the infection takes longer to reach cells further away than in the reference case, and the infection slows down. This could explain the plateau in $\mathcal{R}_0^*$ for $\Delta x = 1, 2, 3$, while the mean time of infection notably dips (see Supplementary Information for details).

3.3. Choice of spatial discretisation influences the time scale of the viral dynamics

So far, we have studied simplified versions of the model in order to pinpoint processes that are influenced by the choice of mesh refinement. We now shift our attention to the full model to examine the effect of spatial discretisation on full, biologically relevant simulations. As a metric by which to compare different simulations, we chose the time of the peak viral load. This quantity is relatively consistent for a given set of parameters (compared to the time to viral extinction, e.g., which is subject to considerable noise) and provides a notion of the aggressiveness of the infection as described by the model. For a range of choices of Δx, we initiated simulations with MOI=0.01 and took the average viral peak time of 32 simulations. As before, we repeated the experiment for both $D = 0.1$ CD^{2}h^{-1} and $D = 1$ CD^{2}h^{-1}.

Fig. 7 shows a plot of the average peak times against values of Δx. Error bars indicate one standard deviation. This plot shows that, provided the diffusion coefficient is sufficiently small, the choice of spatial discretisation can have a substantial impact on the time to peak. Our plot of the mean peak times show that in the small diffusion case, the $\Delta x = 1/6$ and $\Delta x = 6$ cases vary by approximately 9 and 19% respectively compared to the reference case, $\Delta x = 1$.

As in the previous result, Fig. 7 shows that for time to peak, the reference case is an extremum. Both increasing and decreasing the resolution of the mesh results in an acceleration of the infection. This follows from our result that the basic reproduction number of the system is effectively increased in these cases, which in turn is a consequence of our finding that in fine and coarse mesh schemes, viral export from infected cells is enhanced.

Once again, this effect is attenuated when the diffusion coefficient increases, especially relative to the randomness of the system. However, as the inset of Fig. 7 shows, even when the diffusion coefficient is larger ($D = 1$ CD^{2}h^{-1}), a change in Δx still causes an appreciable and consistent variation in the time to peak according to the same trend as in the small diffusion case.

4. Discussion

Spatially-realised models of viral infections within the host represent an opportunity to account for biological detail not possible in ODE models, however, representing the two spatial scales of cells and virus (or other small particles) represents a conceptual challenge (Perelson and Ke, 2021; Gallagher et al., 2018). One popular and "natural" approach to account for these two spatial scales is by coupling a discrete grid of cells to a virus density surface (Sego et al., 2021; Gallagher et al., 2018). Simulating such a system, however, requires the discretisation of the viral density. Here, using a simple but robust model based on standard ODE models of viral dynamics, we have provided a detailed analysis of the effects of this discretisation on model outcomes, subject to various modelling conditions.

In particular, we examined how the behaviour of the model was changed relative to the behaviour of the reference case, where the viral surface is discretised according to the same spacing as the cell grid (that is, where there is one discrete viral node per cell). We showed that, relative to the reference case, both very fine and very coarse mesh refinements both act to accelerate the rate of infections in the model. Note that in the case of refining the mesh this acceleration decreased for

(a)

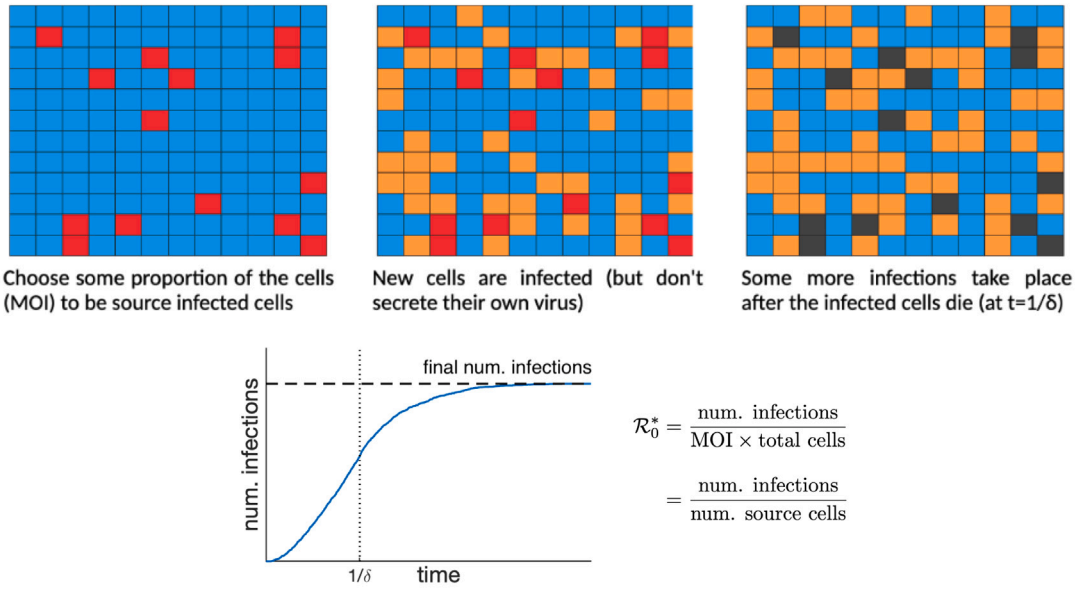

(b)

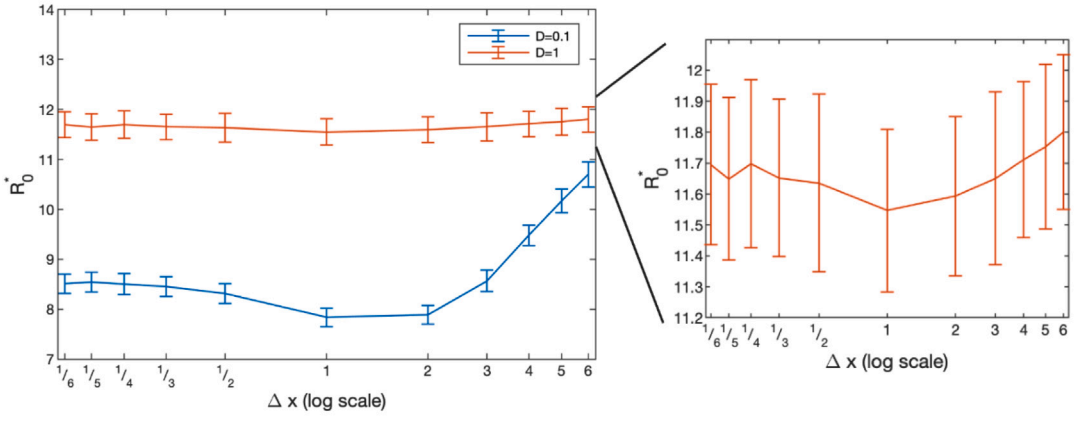

(c)

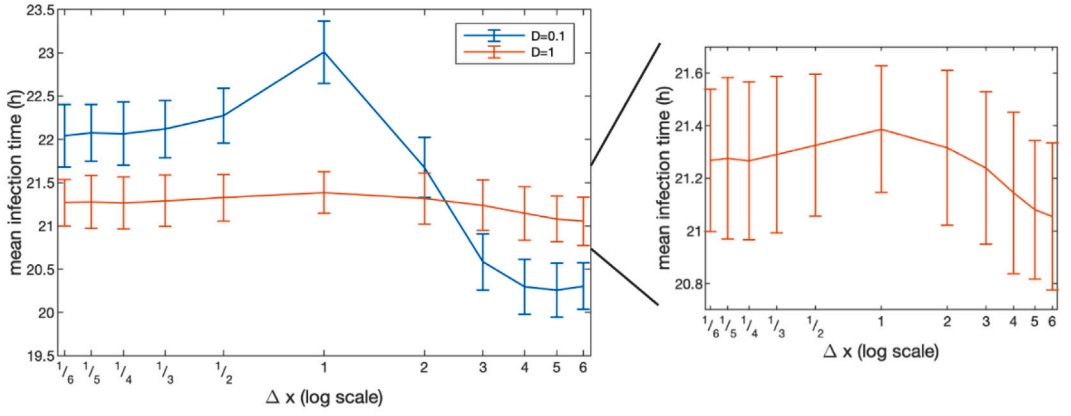

Fig. 6. Spatial discretisation affects the (empirical) basic reproduction number of the model, and causes infections to occur earlier on average. (a) Derivation of the "empirical" basic reproduction number, $\mathcal{R}_0^*$. This quantity measures the average number of infections caused by an infected cell over its lifetime, including infection by virus left in the system after the death of the infected cell. (b) $\mathcal{R}_0^*$ for different choices of mesh refinement (Δx) and diffusion coefficient D. We use a 120 × 120 grid of cells and randomly select 1% of cells as initially infected (MOI = 0.01). We report the mean results of 200 simulations. Error bars indicate one standard deviation. (c) Mean infection times for the simulations in (b).

increasing refinement leading to convergence whereas for coarsening meshes this acceleration continued increasing with increased coarsening. In Fig. 5, we showed that in both of these cases, the rate at which virus leaves the cell from which it is secreted is increased, despite the actual amount of released virus being identical. There are two distinct mechanisms for this behaviour. In the coarse mesh case, the increased rate of viral export is simply explained by the presence of multiple cells that share each viral node (a *plate* of cells). Each cell within a plate has

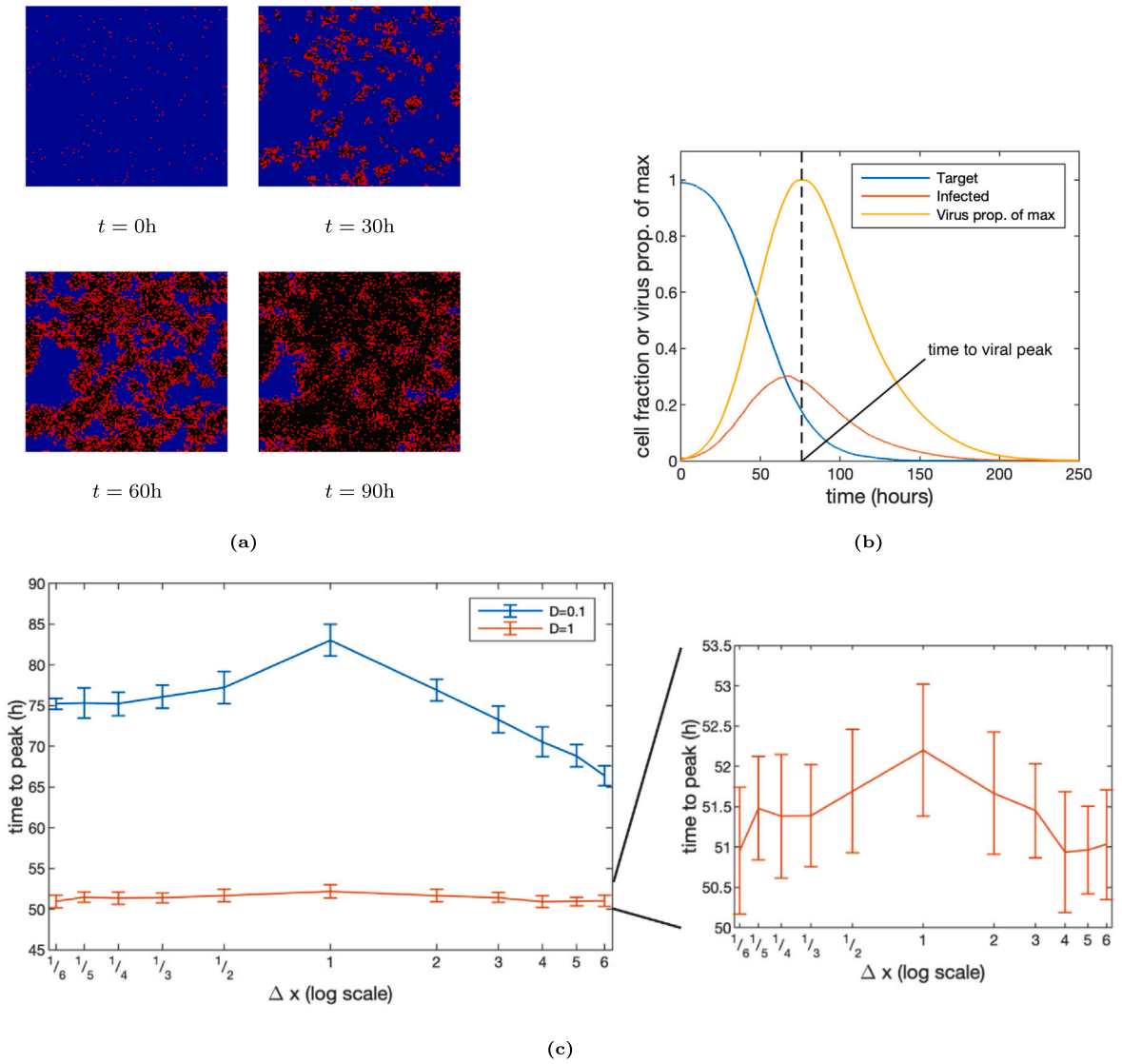

Fig. 7. Time to peak viral load is affected by the choice of spatial discretisation. (a) Cell grid at selected time points in a typical simulation at MOI=0.01 ($D = 0.1$ CD^{2}h^{-1}). Target cells are blue, infected cells are red, and dead cells are black. (b) Net dynamics of the simulation shown in (a). We plot the proportion of cells which are target cells (blue) or infected (red). The total viral load in the system is shown relative to its maximum in yellow. The dashed line represents the time of peak viral load. (c) Time of peak viral load as influenced by choice of Δx for different choices of diffusion coefficient. Here, in each case, we initiate the simulation with MOI=0.01 and perform 32 simulations for each choice of Δx to account for randomness in the model. Error bars reflect one standard deviation either side of the mean.

instantaneous access to virus released from any other cell on the plate, which accelerates transport between local cells and speeds up infection. In the fine mesh case, we hypothesise that the increased rate of viral export is due to the reduction in distance that virus needs to travel to gain access to neighbouring cells. Compared to the reference case – where virus must travel from a viral node at the centre of the secreting cell to another node at the centre of a neighbouring cell – when the mesh is very refined, virus need only reach viral nodes just beyond the cell boundary before that cell experiences viral load.

These two mechanisms impact the "biology" of the model in a complex and non-trivial manner. We introduced the notion of an empirical $\mathcal{R}_0^*$ – analogous to the basic reproduction number $\mathcal{R}_0$ from ODE theory on viral dynamics – to report the number of infections generated by a single infected cell over its lifetime, according to our model and a given set of conditions. We showed that, predictably, $\mathcal{R}_0^*$ was increased relative to the reference case when the mesh was coarsened or refined, however, our analyses revealed that there was minimal increase in the number of infections for Δx values only slightly larger than the reference. This was despite the fact that the average infection time in these simulations was distinctly earlier, and was likely due to constraints on the availability of cells that share a viral node with an initially infected cell.

We also showed the impact that these numerical artefacts have on realistic simulations of our model, using the time to peak viral load as a metric. We found that, once again, compared to the reference case, both fine and coarse meshes led to an earlier time to peak, and therefore suggested a more aggressive infection. Interestingly, here, unlike with $\mathcal{R}_0^*$, there is a clear acceleration in the time to peak even for slightly coarse meshes. This suggests that even though the actual number of infections caused by each infected cell (reproduction number) is much the same, the earlier mean infection time means that new generations of infected cells arise more quickly, and the course of the infection is faster nonetheless. This shows that the relationship between Δx and model outcomes is more complex than merely an increase in infection rates. However, regardless of the mechanism responsible, this change in the time to peak is an important finding of our analysis, since we have shown that if the diffusion coefficient D is small enough, the choice of spatial discretisation can interfere with biologically important outputs of the model, and could have consequences for model predictions and parameter estimations.

The importance of the viral diffusion coefficient, D, has been a recurring theme of our results. In the analysis that we have presented here, we have used two scales of diffusion (the exact values of D are of less importance than their order of magnitude and qualitative influence on the model) and shown repeatedly that in the small diffusion case, the model is much more sensitive to Δx. If the diffusion coefficient is small enough, care must be taken with the choice of spatial discretisation to ensure that numerical solutions converge: our results show that the reference case where viral nodes have the same spacing as cells might not be sufficiently close to the $\Delta x \to 0$ limit. Moreover, in such a scenario, the entire multiscale framework begins to come under strain. We proposed above that the mechanism driving this divergence between the reference case and fine mesh cases was due to a "spill-over" effect, where, if Δx is very small, viral export from an infected cell to its neighbours can be accelerated by reaching nodes only just beyond the cell boundary, as opposed to the single node at its centre in the reference case. Clearly this effect is dependent on the diffusion coefficient being small enough that virus transport over a fraction the width of a cell takes place over a non-trivial time interval. However, should a multiscale model require this level of spatial refinement to converge, this would require a great deal of trust in the spatial arrangement of the cell grid in the model, for example, or in the distribution of viral receptors. Essentially, having very small diffusion under this model framework requires a high degree of detail in the spatial representation of the tissue, to an extent that may exceed the assumptions of a multiscale model.

Clearly, the strength of the results here – and therefore the significance of the spatial discretisation in influencing model dynamics – depends on the rate of viral diffusion. As we mentioned previously, it is difficult to infer the viral diffusion coefficient D from experimental data that is currently available, and this value is likely significantly different in different biological model systems, for example *in vitro* versus *in vivo* contexts. Moreover, it is highly likely that the influence of the viral diffusion coefficient on the structure of infection depends on the values of the other model parameters (β, δ, p and c). We have not explored these in this work, instead opting for indicative values of these parameters, sufficient to show the presence of discretisation influence on model dynamics. However, the uncertainty surrounding the value of D only emphasises the importance of understanding the numerical artefacts which this parameter can impose on the model. We have demonstrated in this work that under a qualitatively meaningful value of the viral diffusion coefficient in the context of our model, $D = 0.1\ \mathrm{CD}^2\mathrm{h}^{-1}$, (which gave rise to familiar ring-shaped infection plaques as shown in Fig. 1), key outcomes of the model – including the computed $\mathcal{R}_0$ and the timescale of infection – depended qualitatively on the choice of spatial discretisation of the viral surface. Furthermore, this dependence of the system on the spatial resolution was so strong that as we have just discussed, the choice of a multicellular framework for the model might be called into question. Those using spatial models in such a context should be aware of this limitation in order to construct models which are not only mathematically consistent (that is, convergent), but which also accurately reflect the underlying assumptions about the spatial structure of the system. This will in turn improve the robustness of biological modelling and inference using such models.

It is worth mentioning one natural approach to addressing this structural limitation, which is to reformulate the model such that viral spread is modelled as a discrete cell-to-cell jumping process, rather than as a continuum diffusion process (in some senses, defining the reference case finite-difference algorithm we have discussed here *as* the model). Our work showed that the behaviour of such a system may differ from a diffusion system under reasonably localised spread, but would have the added advantage of removing the difference in length scale between cells and viruses. On the other hand, such a modelling approach would require explicit representation of an exchange process of viral density between adjacent cells over very small time intervals, which is not supported by existing biological knowledge. Analysis of such a model structure is beyond the scope of this work but a potentially interesting topic of future research.

Since our results depend on the viral diffusion coefficient being relatively small compared to, say, that of small signalling molecules, the scope of our findings applies fairly specifically to viral dynamics. Other modelling contexts where cell dynamics are coupled with diffusing species, of which tumour spheroid models are a good example (e.g., Ghaffarizadeh et al., 2018; Cytowski and Szymanska, 2015), typically consist of diffusing particles much smaller than virions such as oxygen or cytokines that diffuse at much larger rates (Sego et al., 2020). However, unlike the model we have discussed here, even with large diffusion coefficients such models are still spatially structured due to the presence of absorbance or uptake terms (Cytowski and Szymanska, 2015; Sego et al., 2020). Such terms are different to the model framework we have discussed here, and as such our results would need to be reformulated to extend to such systems.

One reason that the diffusion coefficient is difficult to determine may be that the assumption that infections are driven solely by free virus diffusing in the tissue is an oversimplification of the biology. Increasing evidence from the biological literature has suggested that viruses as diverse as herpesviruses, influenza, coronaviruses, retroviruses and hepatitis C can spread between host cells via two distinct but complementary strategies: long-range, extracellular viral spread, and also short-range spread directly between neighbouring cells. Direct cell-to-cell viral spread may progress by a number of mechanisms – including trogocytosis, the formation of syncytia between adjacent cells, and notably, tunnelling nanotubes (TNTs) – that have the common property that virions transmitted in this way do not need to leave the host cell (Tiwari et al., 2021; Kumar et al., 2017; Kongsomros et al., 2021). The movement of such virions are clearly distinct from that of cell-free virions, and therefore may confound the ability to determine D in a diffusion-only model. In future work, we aim to incorporate direct cell-to-cell infection into our model and investigate how this impacts the dynamics of viral spread, particularly in the neighbourhood of infected cells.

In this work we have only considered one size of the tissue, comprising 14,400 cells. There are several reasons for this choice. For one, this domain size is typical for models of the type we discuss here (Sego et al., 2021, 2020; Getz et al., 2020; Blahut et al., 2021), and moreover, for the kinds of parameter sweeps and simulation repetitions necessary for this work, having a much larger domain would incur significant computational costs. However, having a substantially larger cell grid would have interesting consequences for the kind of analysis we conduct here. This is because, with a much larger grid of cells, the balance between the three spatial scales inherent in the model structure – those of the cells, the discretised viral surface, and of the tissue itself – would be fundamentally changed. This would, for example, permit larger values of the viral diffusion coefficient to have non-trivial spatial effects, since, even though the infection front would be diffuse at the scale of tissues discussed in this work, the infection would take some time to spread across the entire sheet. The role that spatial discretisation of the viral surface would play under such a scheme is not clear *a priori*.

This work has only considered the Forward Time Centred Space (FTCS) finite difference method for simulating the viral PDE of our model, using a rectangular discretisation. This choice was due to its simplicity. While it would be infeasible to perform the analysis we have discussed here for all solvers available, the results presented here should follow for other numerical schemes. This is because the mechanisms that we have identified as the likely causes of viral acceleration compared to the reference case (namely, the spill-over effect we described for fine discretisation and the instant transport effect between cells sharing a viral node in the coarse case) are relatively method-agnostic. They depend only on the resolution of spatial detail, and not on the actual representation of spatial structure. In the Supplementary Information, we showed that our results qualitatively hold even for

hexagonal packing of cells and we expect this would also be the case for more general cell packing schemes. We therefore predict that our results would translate straightforwardly to other mesh configurations or solver schemes for the viral PDE such as finite element methods.

A number of works in the viral dynamics literature have identified the need for a greater understanding of model design in spatial models of infection. Early publications by Strain and Funk and their collaborators demonstrated that as the spread of virus in space becomes restricted – analogous to a small diffusion coefficient in our model – model outcomes become more sensitive to spatial effects (Funk et al., 2005; Strain et al., 2002). However, neither study considered a viral density uncoupled from the cells, and therefore investigation of its discretisation in space was not considered. Holder and colleagues conducted a detailed study of, among other features, the value of the viral diffusion coefficient in agent-based models of viral infections (Holder et al., 2011). Their results characterised patterns of spreading infections and described plaque formation in terms of model parameters including the viral diffusion coefficient, however they also avoided explicitly representing the virus distribution in space. Some more general guidance on the design of spatial models of viral dynamics was provided in a review by Gallagher and colleagues (Gallagher et al., 2018). The authors considered a broad range of effects and mechanisms driving spatial spread of infection and provided detailed analysis based on biological data, however stopped short of discussing specific model implementation. More recently, a large multicellular model proposed by Getz and coworkers showed the biological realism possible within the multicellular structure (Getz et al., 2020). The model incorporates a vast array of virological and immunological systems – integrated through the multicellular framework – which makes it possible to simulate the effects of spatially-structured mechanisms such as immune surveillance and the spread of virions and chemical species. This model used a more standard approach to discretisation of the diffusing species by using a finite volume solver, however, the spatial resolution of the solver was not discussed. Sego and collaborators also recently proposed multicellular models for virus dynamics (Sego et al., 2020, 2021). Their work has provided further insight into the role of viral diffusion in these models and developed theory on the changes in model dynamics with the inclusion of spatial structure in viral dynamics models and moreover, their model for SARS-CoV-2 dynamics demonstrates the powerful modelling capability of the multicellular framework (Sego et al., 2020). Their model accounted for a variety of infection outcomes including stochastic extinction or infection rebound – which naturally arise from the structure of the model – whilst also accommodating a high degree of biological detail in the mechanisms of virus and infection spread without relying on neighbour-based infection rules. The model is based on the cellular Potts framework, which allows the discretised viral density to be solved on sub-cellular voxels. The fine resolution of this design potentially avoids the discretisation artefacts we have discussed in this work, however, this comes at the cost of significant increased complexity in the representation of the cell sheet and, as we have already discussed, strong assumptions about the structure of the cell packing and the distribution of viral receptors. Compare this modelling choice to that of other models that use only cell-scale viral data (i.e., the reference case in this work) (Strain et al., 2002; Holder et al., 2011). In this work, we have shown that under biologically realistic parameter settings, the difference in key outcomes of a simple multicellular model – such as the time to viral peak and the computed reproduction number – can vary by as much as 9%. Our work therefore serves to identify and describe the potentially highly important influence the choice of discretisation can have on model outcomes, and therefore enable those who use spatial models of viral dynamics to make informed decisions about model construction and implementation.

Each of the works discussed above demonstrate the crucial role that spatial structure plays in determining system dynamics, and demonstrates in particular the sensitivity of these models to spatial effects when viral spread is highly localised. More recent works show the huge modelling potential afforded by the multicellular structure: that is, in coupling discrete cells to a continuous distribution of extracellular virus (and potentially more diffusing species). However, to our knowledge, nowhere in the literature has the spatial resolution of the discretised viral surface – relative to the cell grid – been properly considered. We have demonstrated in this work that under plausible parameters, the choice of spatial discretisation can in fact qualitatively change biologically meaningful outcomes of even the most foundational multicellular model. We therefore anticipate that more complex models might also be vulnerable to these same effects under reasonable parameters, especially where viral diffusion is small. Our results even suggested that in the worst case scenario where the foundational multicellular model of viral dynamics is especially sensitive to spatial effects, the model may require such a degree of spatial resolution to converge that the multicellular structure may no longer be meaningful, suggesting that there are conditions under which alternative modelling frameworks to the multicellular structure might be preferable. Our work will therefore hopefully provide guidance on the construction of more realistic spatial models of viral infections that incorporate greater biological and immunological detail, helping identify structural concerns that may arise. Future work from our group will continue in this trajectory and examine how spatial structure and spatial spread of viral infections are represented in mathematical models.

CRediT authorship contribution statement

Thomas Williams: Conceptualization, Methodology, Software, Investigation, Writing – original draft. **James M. McCaw:** Conceptualization, Methodology, Supervision, Writing – review & editing. **James M. Osborne:** Conceptualization, Methodology, Supervision, Writing – review & editing.

Declaration of competing interest

The authors declare that they have no known competing financial interests or personal relationships that could have appeared to influence the work reported in this paper.

Acknowledgements

TW is supported by an Australian Government Research Training Program (RTP) scholarship. JMM's research is supported by the Australian Research Council (DP170103076, DP210101920).

Appendix A. Supplementary data

Supplementary material related to this article can be found online at https://doi.org/10.1016/j.jtbi.2023.111592.

References

Baccam, P., Beauchemin, C., Macken, C.A., Hayden, F.G., Perelson, A.S., 2006. Kinetics of influenza a virus infection in humans. J. Virol. 80 (15), 7590–7599. http://dx.doi.org/10.1128/JVI.01623-05.

Beauchemin, C., 2006. Probing the effects of the well-mixed assumption on viral infection dynamics. J. Theoret. Biol. 242 (2), 464–477. http://dx.doi.org/10.1016/j.jtbi.2006.03.014.

Beauchemin, C.A., Handel, A., 2011. A review of mathematical models of influenza a infections within a host or cell culture: lessons learned and challenges ahead. BMC Public Health 11 (1), S7. http://dx.doi.org/10.1186/1471-2458-11-S1-S7.

Blahut, K., Quirouette, C., Feld, J.J., Iwami, S., Beauchemin, C.A.A., 2021. Quantifying the relative contribution of free virus and cell-to-cell transmission routes to the propagation of hepatitis c virus infections in vitro using an agent-based model [preprint]. arXiv, arXiv:2102.05531.

Bocharov, G., Meyerhans, A., Bessonov, N., Trofimchuk, S., Volpert, V., 2016. Spatiotemporal dynamics of virus infection spreading in tissues. PLoS One 11 (12), 1–27. http://dx.doi.org/10.1371/journal.pone.0168576.

Bocharov, G., Meyerhans, A., Bessonov, N., Trofimchuk, S., Volpert, V., 2019. Modelling the dynamics of virus infection and immune response in space and time. Int. J. Parallel Emergent Distrib. Syst. 34 (4), 341–355. http://dx.doi.org/10.1080/17445760.2017.1363203.

Chiem, K., Morales Vasquez, D., Park, J.-G., Platt, R.N., Anderson, T., Walter, M.R., Kobie, J.J., Ye, C., Martinez-Sobrido, L., Parrish, C.R., 2021. Generation and characterization of recombinant SARS-CoV-2 expressing reporter genes. J. Virology 95 (7), e02209–20. http://dx.doi.org/10.1128/JVI.02209-20.

Cytowski, M., Szymanska, Z., 2015. Large-scale parallel simulations of 3D cell colony dynamics: The cellular environment. Comput. Sci. Eng. 17 (5), 44–48. http://dx.doi.org/10.1109/MCSE.2015.66.

Devalia, J.L., Sapsford, R.J., Wells, C.W., Richman, P., Davies, R.J., 1990. Culture and comparison of human bronchial and nasal epithelial cells in vitro. Respir. Med. 84 (4), 303–312. http://dx.doi.org/10.1016/S0954-6111(08)80058-3.

Diekmann, O., Heesterbeek, J.A.P., Roberts, M.G., 2010. The construction of next-generation matrices for compartmental epidemic models. J. R. Soc. Interface 7 (47), 873–885. http://dx.doi.org/10.1098/rsif.2009.0386.

Du, S.Q., Yuan, W., 2020. Mathematical modeling of interaction between innate and adaptive immune responses in COVID-19 and implications for viral pathogenesis. J. Med. Virol. 92 (9), 1615–1628. http://dx.doi.org/10.1002/jmv.25866.

Fukuyama, S., Katsura, H., Zhao, D., Ozawa, M., Ando, T., Shoemaker, J.E., Ishikawa, I., Yamada, S., Neumann, G., Watanabe, S., Kitano, H., Kawaoka, Y., 2015. Multi-spectral fluorescent reporter influenza viruses (color-flu) as powerful tools for in vivo studies. Nature Commun. 6 (1), 6600. http://dx.doi.org/10.1038/ncomms7600.

Funk, G.A., Jansen, V.A., Bonhoeffer, S., Killingback, T., 2005. Spatial models of virus-immune dynamics. J. Theoret. Biol. 233 (2), 221–236. http://dx.doi.org/10.1016/j.jtbi.2004.10.004.

Gallagher, M.E., Brooke, C.B., Ke, R., Koelle, K., 2018. Causes and consequences of spatial within-host viral spread.. Viruses 10 (11), 627. http://dx.doi.org/10.3390/v10110627.

Getz, M., Wang, Y., An, G., Becker, A., Cockrell, C., Collier, N., Craig, M., Davis, C.L., Faeder, J., Versypt, A.N.F., Gianlupi, J.F., Glazier, J.A., Hamis, S., Heiland, R., Hillen, T., Hou, D., Islam, M.A., Jenner, A., Kurtoglu, F., Liu, B., Macfarlane, F., Maygrundter, P., Morel, P.A., Narayanan, A., Ozik, J., Pienaar, E., Rangamani, P., Shoemaker, J.E., Smith, A.M., Macklin, P., 2020. Rapid community-driven development of a SARS-CoV-2 tissue simulator [Pre-print]. http://dx.doi.org/10.1101/2020.04.02.019075.

Ghaffarizadeh, A., Heiland, R., Friedman, S.H., Mumenthaler, S.M., Macklin, P., 2018. PhysiCell: An open source physics-based cell simulator for 3-D multicellular systems. PLoS Comput. Biol. 14 (2), e1005991.

Goyal, A., Cardozo-Ojeda, E.F., Schiffer, J.T., 2020. Potency and timing of antiviral therapy as determinants of duration of SARS-CoV-2 shedding and intensity of inflammatory response. Sci. Adv. 6 (47), http://dx.doi.org/10.1126/sciadv.abc7112.

Graw, F., Martin, D.N., Perelson, A.S., Uprichard, S.L., Dahari, H., Doms, R.W., 2015. Quantification of hepatitis c virus cell-to-cell spread using a stochastic modeling approach. J. Virol. 89 (13), 6551–6561. http://dx.doi.org/10.1128/JVI.00016-15.

Graw, F., Perelson, A.S., 2013. Spatial aspects of HIV infection. In: Ledzewicz, U., Schättler, H., Friedman, A., Kashdan, E. (Eds.), Mathematical Methods and Models in Biomedicine. Springer New York, New York, NY, pp. 3–31. http://dx.doi.org/10.1007/978-1-4614-4178-6{_}1.

Guedj, J., Dahari, H., Rong, L., Sansone, N.D., Nettles, R.E., Cotler, S.J., Layden, T.J., Uprichard, S.L., Perelson, A.S., 2013. Modeling shows that the NS5A inhibitor daclatasvir has two modes of action and yields a shorter estimate of the hepatitis C virus half-life. Proc. Natl. Acad. Sci. USA 110 (10), 3991–3996. http://dx.doi.org/10.1073/pnas.1203110110.

Hernandez-Vargas, E.A., Velasco-Hernandez, J.X., 2020. In-host mathematical modelling of COVID-19 in humans. Ann. Rev. Control 50, 448–456. http://dx.doi.org/10.1016/j.arcontrol.2020.09.006.

Holder, B.P., Liao, L.E., Simon, P., Boivin, G., Beauchemin, C.A.A., 2011. Design considerations in building in silico equivalents of common experimental influenza virus assays. Autoimmunity 44 (4), 282–293. http://dx.doi.org/10.3109/08916934.2011.523267.

Jenner, A.L., Aogo, R.A., Alfonso, S., Crowe, V., Deng, X., Smith, A.P., Morel, P.A., Davis, C.L., Smith, A.M., Craig, M., 2021. COVID-19 virtual patient cohort suggests immune mechanisms driving disease outcomes. PLOS Pathog. 17 (7), 1–33. http://dx.doi.org/10.1371/journal.ppat.1009753.

Kongsomros, S., Manopwisedjaroen, S., Chaopreecha, J., Wang, S.-F., Borwornpinyo, S., Thitithanyanont, A., 2021. Rapid and efficient cell-to-cell transmission of avian influenza H5N1 virus in MDCK cells is achieved by trogocytosis. Pathogens 10 (4), http://dx.doi.org/10.3390/pathogens10040483, URL https://www.mdpi.com/2076-0817/10/4/483.

Kumar, A., Kim, J.H., Ranjan, P., Metcalfe, M.G., Cao, W., Mishina, M., Gangappa, S., Guo, Z., Boyden, E.S., Zaki, S., York, I., García-Sastre, A., Shaw, M., Sambhara, S., 2017. Influenza virus exploits tunneling nanotubes for cell-to-cell spread. Sci. Rep. 7, 40360. http://dx.doi.org/10.1038/srep40360, URL https://pubmed.ncbi.nlm.nih.gov/28059146.

Kumberger, P., Durso-Cain, K., Uprichard, S.L., Dahari, H., Graw, F., 2018. Accounting for space—Quantification of cell-to-cell transmission kinetics using virus dynamics models. Viruses 10 (4), 200. http://dx.doi.org/10.3390/v10040200.

Lax, P.D., Richtmyer, R.D., 1956. Survey of the stability of linear finite difference equations. Comm. Pure Appl. Math. 9 (2), 267–293. http://dx.doi.org/10.1002/cpa.3160090206, URL https://doi.org/10.1002/cpa.3160090206.

Levin, D., Forrest, S., Banerjee, S., Clay, C., Cannon, J., Moses, M., Koster, F., 2016. A spatial model of the efficiency of t cell search in the influenza-infected lung. J. Theoret. Biol. 398, 52–63. http://dx.doi.org/10.1016/j.jtbi.2016.02.022.

Michael Lavigne, G., Russell, H., Sherry, B., Ke, R., 2021. Autocrine and paracrine interferon signalling as 'ring vaccination' and 'contact tracing' strategies to suppress virus infection in a host. Proc. R. Soc. B 288 (1945), 20203002. http://dx.doi.org/10.1098/rspb.2020.3002.

Neumann, A.U., Lam, N.P., Dahari, H., Gretch, D.R., Wiley, T.E., Layden, T.J., Perelson, A.S., 1998. Hepatitis c viral dynamics in vivo and the antiviral efficacy of interferon-alpha therapy. Science 282 (5386), 103–107. http://dx.doi.org/10.1126/science.282.5386.103.

Paiva, L.R., Binny, C., Ferreira, S.C., Martins, M.L., 2009. A multiscale mathematical model for oncolytic virotherapy. Cancer Res. http://dx.doi.org/10.1158/0008-5472.CAN-08-2173.

Perelson, A.S., 2002. Modelling viral and immune system dynamics. Nat. Rev. Immunol. 2 (1), 28–36. http://dx.doi.org/10.1038/nri700.

Perelson, A., Ke, R., 2021. Mechanistic modeling of SARS-CoV-2 and other infectious diseases and the effects of therapeutics. Clin. Pharmacol. Therapeut. 209 (4), 829–840. http://dx.doi.org/10.1002/cpt.2160.

Quirouette, C., Younis, N.P., Reddy, M.B., Beauchemin, C.A.A., 2020. A mathematical model describing the localization and spread of influenza a virus infection within the human respiratory tract.. PLoS Comput. Biol. 16 (4), e1007705. http://dx.doi.org/10.1371/journal.pcbi.1007705.

Rodriguez-Brenes, I.A., Hofacre, A., Fan, H., Wodarz, D., 2017. Complex dynamics of virus spread from low infection multiplicities: Implications for the spread of oncolytic viruses. PLoS Comput. Biol. 13 (1), e1005241.

Sego, T., Aponte-Serrano, J.O., Gianlupi, J.F., Glazier, J.A., 2021. Generating agent-based multiscale multicellular spatiotemporal models from ordinary differential equations of biological systems, with applications in viral infection [Pre-print]. http://dx.doi.org/10.1101/2021.01.28.428647.

Sego, T.J., Aponte-Serrano, J.O., Gianlupi, J.F., Heaps, S.R., Breithaupt, K., Brusch, L., Crawshaw, J., Osborne, J.M., Quardokus, E.M., Plemper, R.K., Glazier, J.A., 2020. A modular framework for multiscale, multicellular, spatiotemporal modeling of acute primary viral infection and immune response in epithelial tissues and its application to drug therapy timing and effectiveness. PLoS Comput. Biol. 16 (12), e1008451. http://dx.doi.org/10.1371/journal.pcbi.1008451.

Smith, A.M., Perelson, A.S., 2011. Influenza a virus infection kinetics: quantitative data and models.. Wiley Interdiscip. Rev. Syst. Biol. Med. 3 (4), 429–445. http://dx.doi.org/10.1002/wsbm.129.

Strain, M.C., Richman, D.D., Wong, J.K., Levine, H., 2002. Spatiotemporal dynamics of HIV propagation. J. Theoret. Biol. 218 (1), 85–96. http://dx.doi.org/10.1006/jtbi.2002.3055.

Tiwari, V., Koganti, R., Russell, G., Sharma, A., Shukla, D., 2021. Role of tunneling nanotubes in viral infection, neurodegenerative disease, and cancer. Front. Immunol. 12, 2256. http://dx.doi.org/10.3389/fimmu.2021.680891, URL https://www.frontiersin.org/article/10.3389/fimmu.2021.680891.

Whitman, J., Dhanji, A., Hayot, F., Sealfon, S.C., Jayaprakash, C., 2020. Spatio-temporal dynamics of host-virus competition: A model study of influenza a.. J. Theoret. Biol. 484, 110026. http://dx.doi.org/10.1016/j.jtbi.2019.110026.

Wodarz, D., Hofacre, A., Lau, J.W., Sun, Z., Fan, H., Komarova, N.L., 2012. Complex spatial dynamics of oncolytic viruses in vitro: Mathematical and experimental approaches. PLoS Comput. Biol. 8 (6), e1002547. http://dx.doi.org/10.1371/journal.pcbi.1002547.